



# X-ray Computed Tomography Studies on Porosity Distribution in Vacuum Induction Cast Al-7Si Alloys

JAMES MATHEW,<sup>1</sup> MARK A. WILLIAMS,<sup>1</sup> and PRAKASH SRIRANGAM<sup>1,2</sup>

1.—Warwick Manufacturing Group, University of Warwick, Coventry CV4 7AL, UK.  
2.—e-mail: p.srirangam@warwick.ac.uk

Porosity in aluminum alloys is a great concern to the casting and automotive industry. In this publication, porosity formation in air-melted and vacuum induction melted (VIM) aluminum alloys was studied and compared to understand its effect on microstructure and mechanical properties of Al-7Si alloys. Al-7Si alloys were cast at 700°C and 900°C in a muffle furnace and VIM furnace. Microstructural results show that the alloys cast in muffle furnace refined the eutectic silicon compared with the cast samples prepared in VIM furnace. X-ray computed tomography (XCT) was used for three-dimensional (3D) visualization and quantification of porosity in these alloys. The volume fraction of pores was observed to be higher in alloy air-melted at 900°C compared with 700°C. XCT results from VIM alloy samples showed no significant porosity when cast at either 700°C or 900°C. The morphology of large pores in alloys air-melted at 700°C represents the formation of shrinkage porosity due to the incomplete flow of molten metal during solidification. Tensile test results show that the elongation property of VIM alloy was increased by more than 20% compared with air-melted alloy. The tensile strength and elongation were observed to be higher for alloy samples cast at 700°C compared with 900°C for both air-melted and VIM alloys. The findings from microstructure, XCT, and tensile tests show that vacuum induction melting improves the mechanical properties of the alloy compared with air-melted alloy.

## INTRODUCTION

Aluminum-silicon alloys are widely used in automotive, aerospace, communication, and domestic casting applications due to their high strength to weight ratio, high thermal conductivity, high formability, and corrosion resistance.<sup>1–3</sup> However, porosity formation in cast aluminum alloys is a significant concern as it deteriorates the mechanical properties.<sup>4</sup> Melt treatment of aluminum alloys plays an important role in aluminum castings. Melt treatment dissolves all the heterogeneities in molten metal and prevents their growth and the formation of new heterogeneities, thereby improving the overall properties.<sup>5</sup> Melt treatment processes are generally of three types: thermal treatments (superheating, fast cooling, and heat

treatment), physical and mechanical treatments (using vacuum, ultrasonic vibration, electromagnetic fields, stirring, etc.), and chemical methods (addition of modifiers or grain refiners to the melt).<sup>6</sup>

Among these methods, melt superheating is an industrially viable melt treatment method in aluminum castings due to its ease of application compared with other methods. The setup cost of other thermal, physical, and mechanical processing techniques is relatively high, and chemical additions are less economical than melt superheating methods.<sup>7</sup> It has been reported that melting and casting at high superheat temperatures results in the dissolution of harmful heterogeneities and the formation of fine-grain microstructure in alloys.<sup>5,8–10</sup> Wang et al.<sup>11</sup> reported that an increase in undercooling with increase in superheat temperature results in the formation of equiaxed and nearly globular silicon crystals in Al-Si alloys.<sup>12</sup> However, higher superheating temperatures have disadvantages such as higher energy consumption, furnace

(Received July 15, 2021; accepted September 23, 2021;  
published online October 26, 2021)

To reduce the exposure to the atmosphere and hydrogen during melting and solidification of molten metal, vacuum induction melting (VIM) and solidification of Al-Si alloy was investigated in this work. VIM is viable industrially because of its independent control of time, temperature, pressure, and mass transport by melt stirring.<sup>15</sup> VIM also offers several advantages such as ease of operation, low oxidation losses, precise control of temperature, low level of environmental pollution from dust output, removal of impurity elements with high vapor pressures on recycling scrap, removal of dissolved gases, etc.<sup>15</sup> Nowadays, vacuum-assisted castings are gaining importance in the casting and automotive industries because of their ability to decrease porosity formation and improve mechanical properties.<sup>16-18</sup> Hence, it is essential to compare the porosity formation and its effect on the mechanical properties of Al-Si alloys prepared by the vacuum induction melting versus air melting method. In this publication, the effect of vacuum melting and casting of Al-7Si alloys at different superheating temperatures on porosity formation and mechanical properties is studied. Further, 3D x-ray tomography to visualize and quantify porosity in air-melted and VIM cast Al-7Si alloys is presented and discussed.

The tensile samples were scanned before and after the test using the Zeiss versa at CiMat, WMG, University of Warwick, UK. Samples were prepared

[illegible]

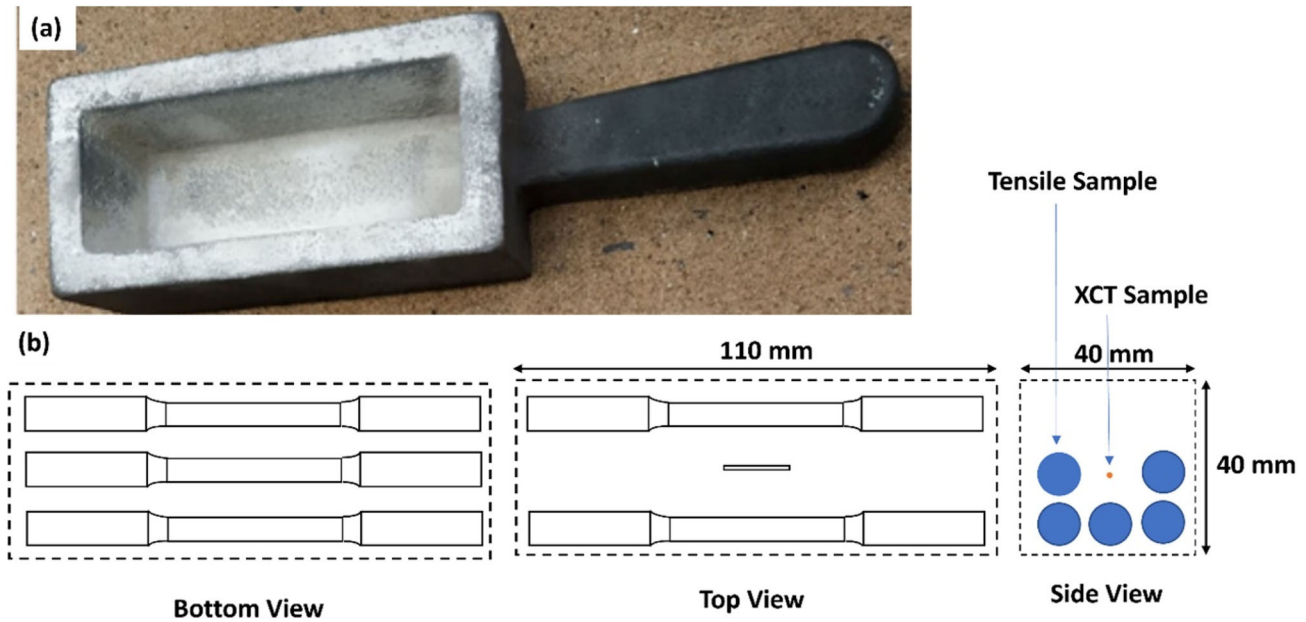


Fig. 1. Alloy preparation: (a) cast-iron mold, (b) schematic showing sample locations from where samples were taken for XCT measurements and tensile tests.

**Table II. X-ray tomography scanning parameters**

Scanning condition	Zeiss versa
Voltage (kV)	80
Current ( $\mu$ A)	87
Number of projections	1601
Filtration	LE4
Voxel size ( $\mu$ m)	3.67

as 1-mm-diameter cylinders and scanned under the conditions given in Table II. The sampling position of the specimen for CT investigation is shown in Fig. 1b (top view and side view). To achieve the best resolution possible, a  $0.4\times$  flat panel was used as the detector, composed of  $2048 \times 2048$  pixels resulting in resolution of  $3.67 \mu\text{m}$ . The raw data were reconstructed using the Zeiss reconstruction software that uses the filtered back-projection (FBP) algorithm, creating a stack of DICOM images. The stack can then be used for analysis with Avizo 9.4.0 (FEI, USA; <http://www.fei.com/software/avizo3d>).

### Mechanical Property Characterization

Cylindrical tensile samples were prepared using a CNC lathe according to the dimensions specified in ASTM E-8M.<sup>19</sup> The sampling position of tensile specimens is shown in Fig. 1b. Tensile properties were evaluated using a 100 kN universal tensile testing machine (Instron model 5800R) at a 2 mm/min constant crosshead speed. The measurements were taken on five samples for each condition, and

the average value was used in determining the tensile properties of the alloys. The fracture surface was then studied using a Zeiss sigma SMT AG instrument.

### Results and Discussion

Figure 2 shows optical microscopy images of the Al-7Si alloy cast in air at temperatures of  $700^\circ\text{C}$  and  $900^\circ\text{C}$ , respectively.

Figure 3 shows optical microscopy images of Al-7Si alloy cast under vacuum at melt temperature of  $700^\circ\text{C}$  or  $900^\circ\text{C}$ . There were no visible pores in either condition. This was due to the vacuum conditions for the casting, which prevents oxidation and vaporizes the gases present in the raw materials, allowing them to escape from the molten alloy.

The optical microstructure images show that the Al-7Si alloy cast in air had a finer microstructure than when cast under vacuum conditions. The average size of silicon particles was observed to be larger in vacuum cast alloy (Fig. 3) compared with air-melted alloy (Fig. 2). Also, the space between silicon particles was greater in vacuum cast alloy.

Figure 4 shows 3D reconstructed x-ray CT images of Al-7Si alloy cast in air at  $700^\circ\text{C}$  or  $900^\circ\text{C}$ . The 1-mm cylindrical samples were scanned using x-ray CT, and the two-dimensional (2D) images were stacked together to reconstruct three-dimensional (3D) images. The largest possible cuboid-shaped subsamples were cropped out from these 3D cylindrical images to remove the outside border of the cylinder, which has a distinctive contrast. The gray-colored structure represents the aluminum matrix, while blue-colored features represent the porosity. In air melting, the molten metal surface was

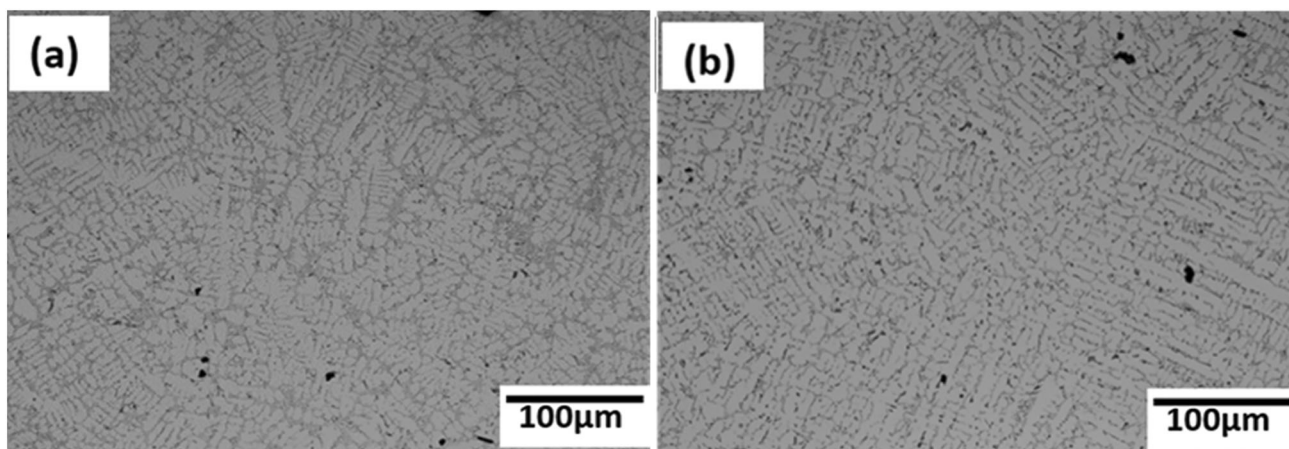


Fig. 2. Optical microstructure of Al-7Si alloys cast at (a) 700°C and (b) 900°C in air.

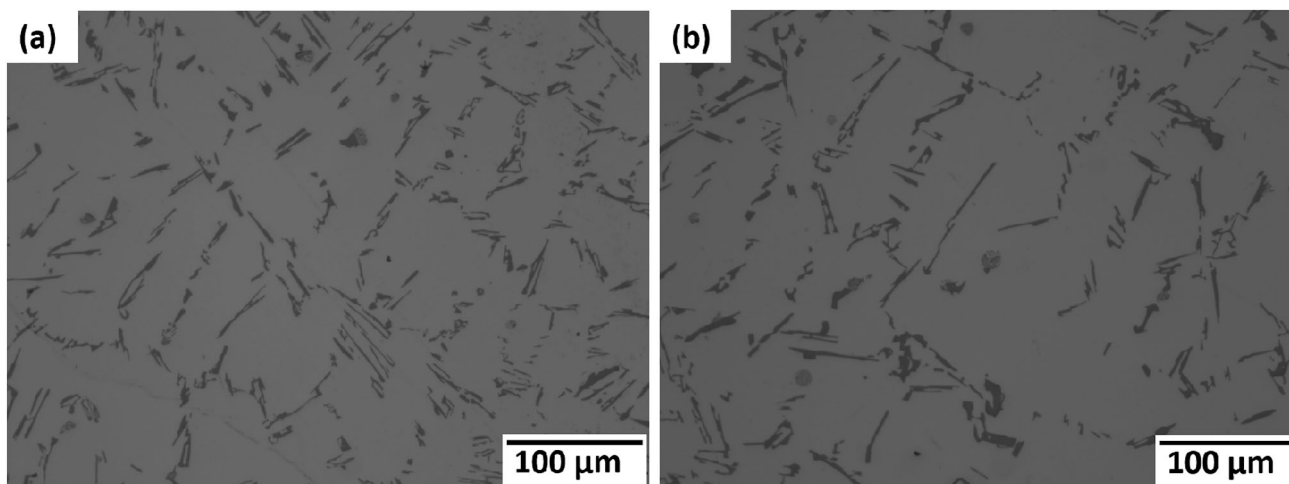


Fig. 3. Optical microstructure of Al-7Si alloys cast at (a) 700°C and (b) 900°C in vacuum induction furnace.

exposed to the outside atmosphere and reacts with moisture present in the atmosphere. This resulted in the formation of hydrogen, which dissolves in the aluminum melt and later escapes during solidification, resulting in the formation of porosity.<sup>4</sup>

It is evident from Fig. 4a and b that the alloy cast at 900°C appeared to have a higher number of pores compared with the alloy cast at 700°C in air melt conditions. This could be due to the increase in the solubility of hydrogen in molten aluminum with increasing superheat temperature.<sup>20</sup> Also, the shape of the pores appears to be spherical in the air-melted alloy at 900°C, while most pores seem to be jagged or linear in shape in the alloy air-melted at 700°C. Spherical morphology generally represents gas porosity, while linear morphology represents shrinkage porosity.<sup>21</sup> These shrinkage pores in the Al-7Si alloy air-melted at 700°C could be due to restriction of the flow of molten metal around the silicon flakes during solidification. Casting at 900°C helped to increase the fluidity of the molten metal

and the refinement of eutectic silicon flakes, as observed in the optical microstructure with high level of undercooling, thereby reducing the chances of formation of shrinkage porosity.

Figure 5 shows 3D reconstructed x-ray CT images from Al-7Si cast under vacuum at melt temperature of 700°C or 900°C. It is evident from Fig. 4a that the alloy melted at 700°C in vacuum condition showed no porosity. However, some tiny pores were present in the alloy melted at 900°C even in vacuum conditions, which could be due to the increase in the superheat temperature of the alloy, as shown in Fig. 5b.

Figure 6 shows the quantification of the pores formed in Al-7Si alloy cast under vacuum and air-melted at temperature of 700°C or 900°C. The pores below the size range of 1 μm were neglected as noise present in the imaging or processing. Considering the number of porosities above 10 μm size, there was no reported porosities in Al-7Si cast in vacuum induction furnace, whereas there were more than 50



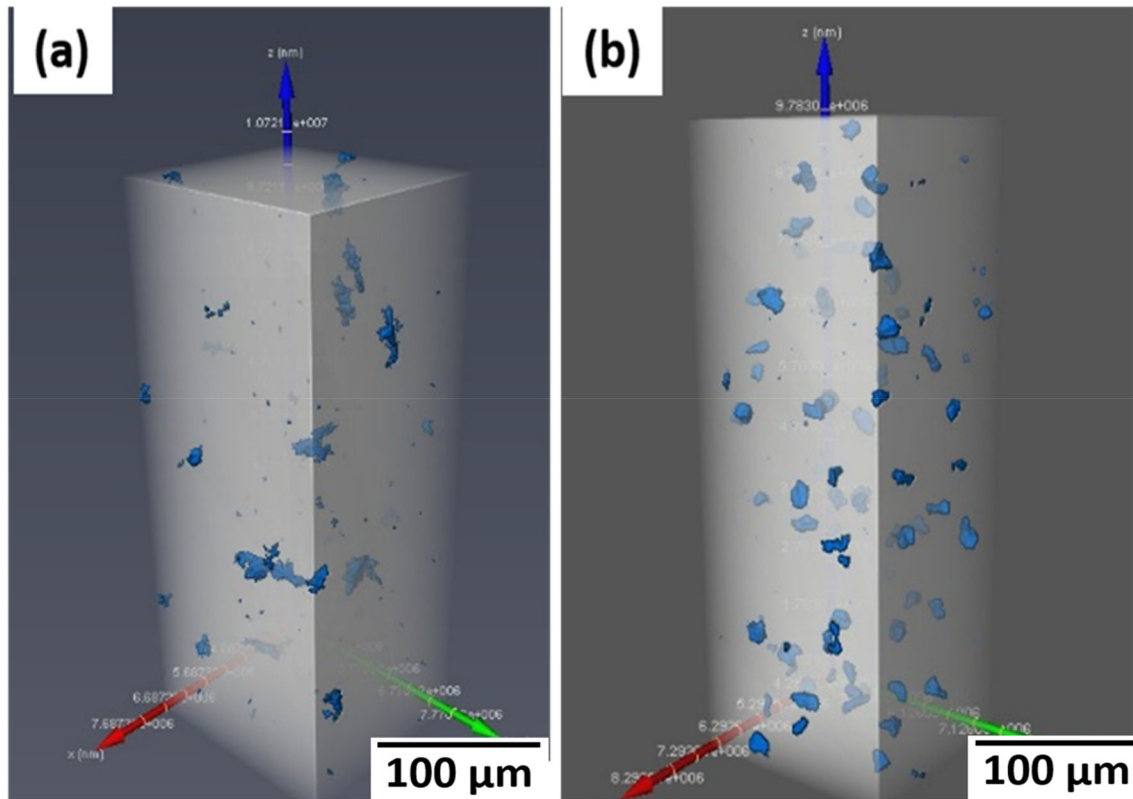


Fig. 4. 3D reconstructed CT images of Al-7Si alloy air-melted at (a) 700°C and (b) 900°C.

pores above 10  $\mu\text{m}$  size in the alloys cast in air. This represents the effect of vacuum cast in reducing the formation of porosity in Al-7Si alloys.

The 3D XCT results show that the porosity formation in vacuum conditions was significantly lower than in air melting conditions. Therefore, it was necessary to evaluate the tensile properties to study the effect of vacuum conditions in defining the mechanical properties of the alloy. Figure 7 shows the tensile stress versus strain curves of Al-7Si alloys cast at 700°C and 900°C in the air melting and vacuum conditions. The tensile curves of Al-7Si alloys show that the tensile stress for the alloys cast in open atmospheric conditions was slightly better than that of alloys cast in a vacuum furnace. This may be due to silicon refinement of Al-7Si alloys cast in air. The values of the tensile strength and elongation, along with their standard deviations, are presented in Table III. The strain/elongation was lower for the alloy cast in the air than the vacuum induction casting. This may be due to the reduced porosity on vacuum casting compared with air melting. The tensile curves of air-melted Al-7Si alloy show that the maximum tensile stress and strain were observed to be higher when superheating at 700°C compared with 900°C. This may be due to the early failure of alloys cast at 900°C resulting from a high volume fraction of pores. Therefore, vacuum induction melting is suitable for alloys that

require excellent elongation properties without compromising their ultimate tensile strength. Moreover, from the standard deviation values observed in Table III, the tensile properties of the alloys were observed to be more consistent for the vacuum melted than air-melted alloys. This could be due to the higher percentage of porosity that resulted in random failures of tensile specimens in the air-melted alloys.

The present study using the XCT technique and tensile testing indicates that the application of vacuum induction melting reduces the porosity in Al-7Si alloy and helps improve the mechanical properties. The 3D visualization and quantified data of porosity obtained from the XCT results are helpful for understanding the effect of vacuum conditions in melting and casting and useful for modeling the properties of alloys with and without porosity.

## CONCLUSION

- Al-7Si alloys were prepared in air-melted and vacuum conditions at two different superheat temperatures (700°C and 900°C).
- Increasing the superheat temperature resulted in refinement of silicon particles but also increased the formation of porosity in the alloys.

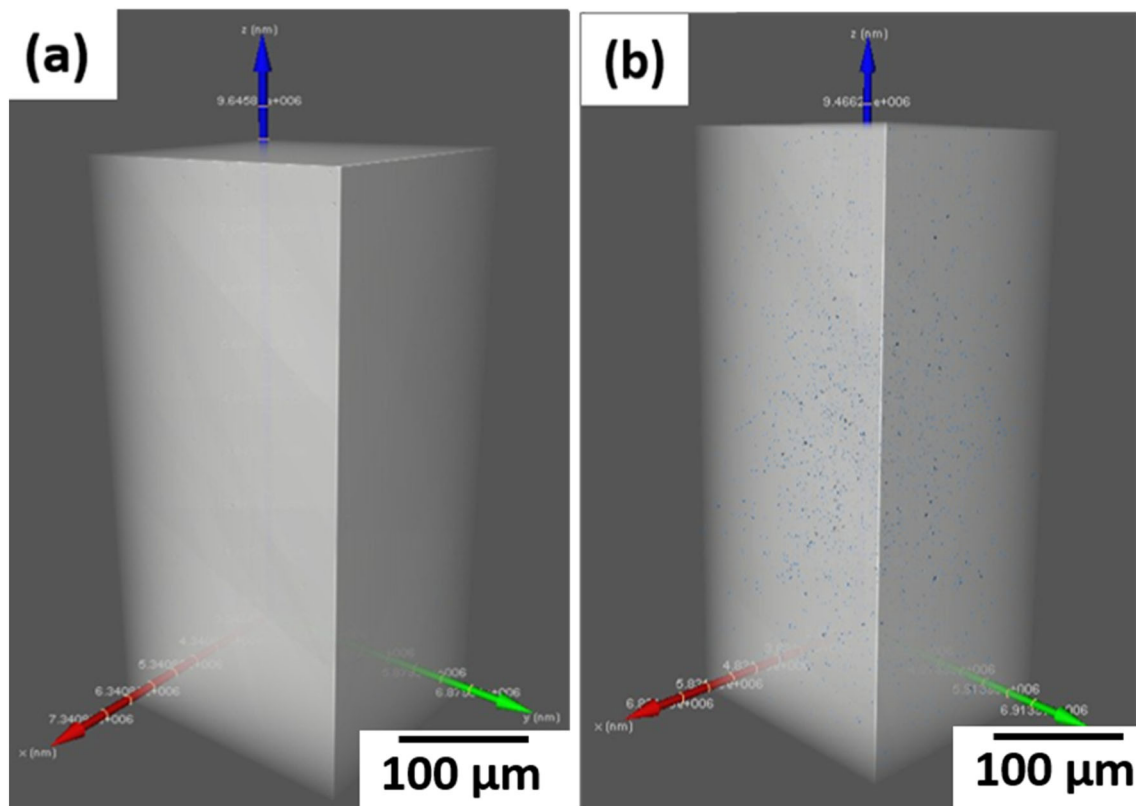


Fig. 5. 3D reconstructed CT images of Al-7Si vacuum cast alloy at (a) 700°C and (b) 900°C.

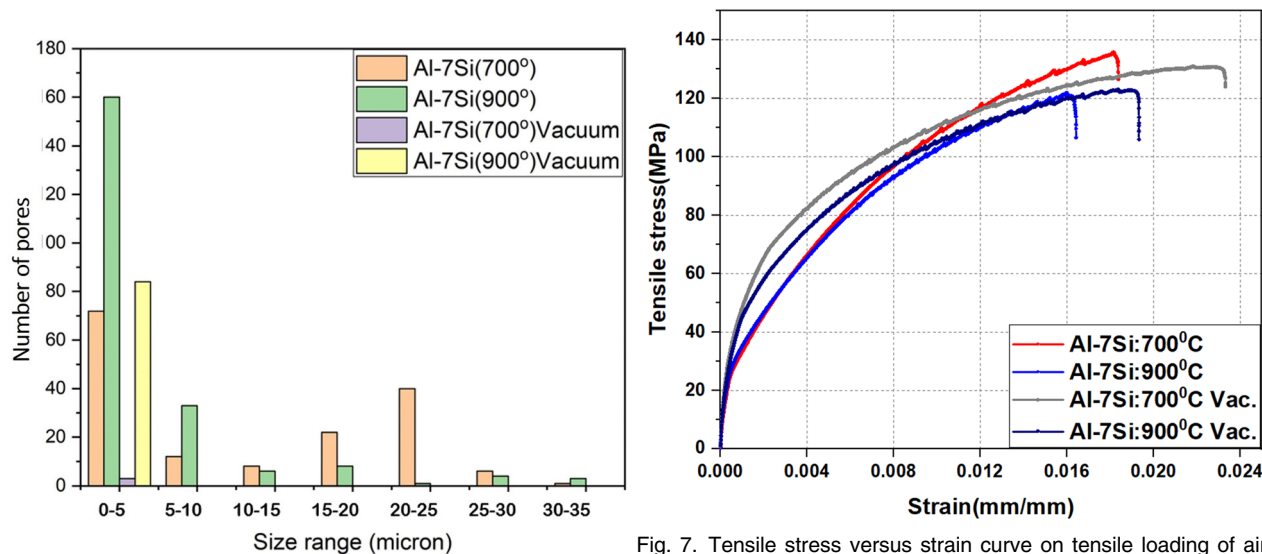


Fig. 6. Size distribution of porosity in Al-7Si alloys vacuum cast and air-melted at 700°C and 900°C.

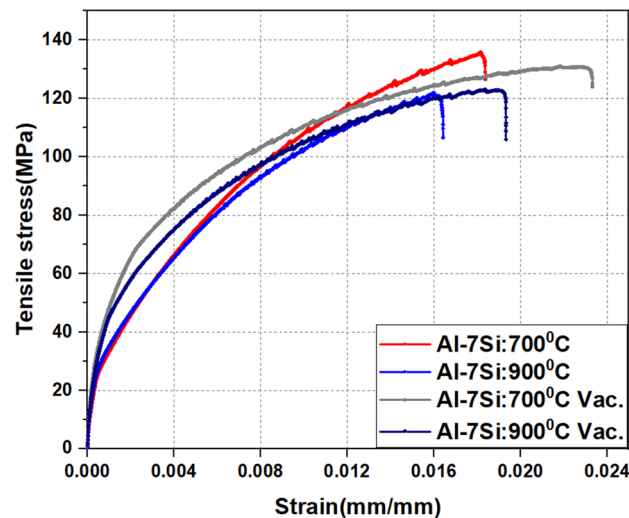


Fig. 7. Tensile stress versus strain curve on tensile loading of air-melted and vacuum cast Al-7Si alloys.

**Table III. Tensile test results: strength and elongation property values for each condition**

Alloy	Tensile strength	SD	Elongation	SD
Al-7Si: 700°C vacuum cast	130.79	± 0.21	4.58	± 0.02
Al-7Si: 900°C vacuum cast	126.51	± 0.75	3.75	± 0.03
Al-7Si: 700°C air-melted	133.83	± 2.34	3.64	± 0.35
Al-7Si: 900°C air-melted	124.95	± 2.36	3.31	± 0.32

Application of vacuum helped immensely in reducing the porosity formation in Al-7Si alloy and helped improve the elongation properties of the alloys compared with air-melted alloys.

### CONFLICT OF INTEREST

All authors declare that they have no conflict of interest.

### OPEN ACCESS

This article is licensed under a Creative Commons Attribution 4.0 International License, which permits use, sharing, adaptation, distribution and reproduction in any medium or format, as long as you give appropriate credit to the original author(s) and the source, provide a link to the Creative Commons licence, and indicate if changes were made. The images or other third party material in this article are included in the article's Creative Commons licence, unless indicated otherwise in a credit line to the material. If material is not included in the article's Creative Commons licence and your intended use is not permitted by statutory regulation or exceeds the permitted use, you will need to obtain permission directly from the copyright holder. To view a copy of this licence, visit <http://creativecommons.org/licenses/by/4.0/>.

### REFERENCES

1. K. Li, J. Zhang, X. Chen, Y. Yin, Y. He, Z. Zhou, and R. Guan, *J. Mater. Res. Technol.* 9, 8780. <https://doi.org/10.1016/j.jmrt.2020.06.021> (2020).
2. A. Darlapudi, S.D. McDonald, S. Terzi, A. Prasad, M. Felberbaum, and D.H. StJohn, *J. Cryst. Growth* 433, 63. <https://doi.org/10.1016/j.jcrysgro.2015.10.002> (2016).
3. R.N. Lumley, N. Deeva, R. Larsen, J. Gembarovic, and J. Freeman, *Metall Mater. Trans. A Phys. Metall. Mater. Sci.* 44, 1074. <https://doi.org/10.1007/s11661-012-1443-7> (2013).
4. J. Zeng, B. Wu, Z. Hu, L. Wang, and D. Cao, *Light Met.* ed. Grandfield, J. (Springer, Cham, 2014), p. 1051. <https://doi.org/10.1002/9781118888438.ch175>.
5. P. Li, V.I. Nikitin, E.G. Kandalova, and K.V. Nikitin, *Mater. Sci. Eng. A* 332, 371. [https://doi.org/10.1016/S0921-5093\(01\)01864-0](https://doi.org/10.1016/S0921-5093(01)01864-0) (2002).
6. K.V. Nikitin, V.I. Nikitin, I.Y. Timoshkin, D.S. Krivopalov, and D.G. Chernikov, *Russ. J. Non-Ferrous Met.* 56, 20. <https://doi.org/10.3103/S1067821215010137> (2015).
7. W. Yang, X. Yang, and S. Ji, *Met. Mater. Int.* 21, 382. <https://doi.org/10.1007/s12540-015-4215-2> (2015).
8. X. Bian, and W. Wang, *Mater. Lett.* 44, 54. [https://doi.org/10.1016/S0167-577X\(00\)00011-2](https://doi.org/10.1016/S0167-577X(00)00011-2) (2000).
9. H. Chiriac, F. Vinai, M. Tomut, A. Stantero, and E. Ferarra, *J. Non. Cryst. Solids* 250, 709. [https://doi.org/10.1016/S0022-3093\(99\)00165-9](https://doi.org/10.1016/S0022-3093(99)00165-9) (1999).
10. N.K. Prasad, P.K. Kumar, A. Sharma, and M.K. Bhargava, *Indian Foundry J.* 60, 23. (2014).
11. R. Wang and W. Lu, *Electrolysis*, ed. Janis Kleperis and Vladimir Linkov (Intech, Rijeka, 2012), pp. 107–140. <http://doi.org/10.5772/52962>.
12. R. Y. Wang, W. H. Lu, and Z. Y. Ma, *Light Metals*, ed. T.J. Galloway (Warrendale, PA: TMS, 2006) pp. 819–824. [https://www.researchgate.net/profile/Ru-YaoWang/publication/268203800\\_Hypereutectic\\_Al-Si\\_alloy\\_castings\\_with\\_a\\_completely\\_eutectic\\_structure/links/548ec7050cf2d1800d845497/Hypereutectic-Al-Si-alloy-castings-with-a-completely-eutectic-structure.pdf](https://www.researchgate.net/profile/Ru-YaoWang/publication/268203800_Hypereutectic_Al-Si_alloy_castings_with_a_completely_eutectic_structure/links/548ec7050cf2d1800d845497/Hypereutectic-Al-Si-alloy-castings-with-a-completely-eutectic-structure.pdf).
13. D.G. Eskin, K. Al-Helal, and I. Tzanakis, *J. Mater. Process. Technol.* 222, 148. <https://doi.org/10.1016/j.jmatprotec.2015.03.006> (2015).
14. J. Zeng, P. Gu, and Y. Wang, *Mater. Sci. Eng. B* 177, 1717. <https://doi.org/10.1016/j.mseb.2012.02.005> (2012).
15. *ASM Handbook vol. 15*, ed. S. Viswanathan, D. Apelian, R.J. Donahue, B.D. Gupta, M. Gwyn, J.L. Jorstad, R.W. Monroe, M. Sahoo, T.E. Prucha and D. Twarog (ASM International, Materials Park, OH, USA, 2008), pp. 1–8. <https://doi.org/10.1361/asmhba0005200>.
16. I.G. Chung, A. Bolouri, and C.G. Kang, *Int. J. Adv. Manuf. Technol.* 58, 237. <https://doi.org/10.1007/s00170-011-3376-5> (2012).
17. X. Dong, X. Zhu, and S. Ji, *J. Mater. Process. Technol.* 266, 105. <https://doi.org/10.1016/j.jmatprotec.2018.10.030> (2018).
18. H. Cao, M. Hao, C. Shen, and P. Liang, *Vacuum* 146, 278. <https://doi.org/10.1016/j.vacuum.2017.09.048> (2017).
19. ASTM Int., *Astm* (2009), pp. 1–27. <https://www.astm.org/Standards/E8.htm>.
20. M. Li, D.G. Xie, E. Ma, J. Li, X.X. Zhang, and Z.W. Shan, *Nat. Commun.* 8, 1. <https://doi.org/10.1038/ncomms14564> (2017).
21. S.G. Lee and A.M. Gokhale, *Scr. Mater.* 55, 387. <https://doi.org/10.1016/j.scriptamat.2006.04.040> (2006).

**Publisher's Note** Springer Nature remains neutral with regard to jurisdictional claims in published maps and institutional affiliations.